The angle-dependent phase velocity of GHz acoustic waves in GaAs

Wohlfarth, Maja

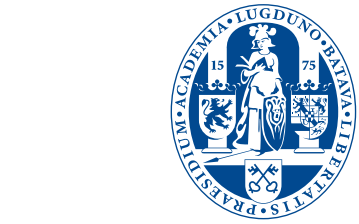

The angle-dependent phase velocity of GHz acoustic waves in GaAs

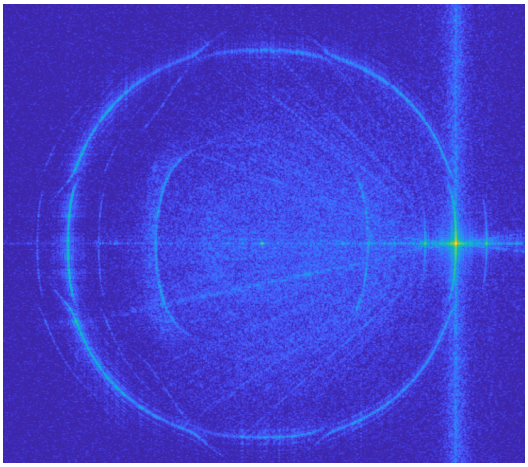

THESIS

submitted in partial fulfillment of the
requirements for the degree of

MASTER OF SCIENCE
in
PHYSICS

Author :	Maja Wohlfarth
Student ID :	s3894711
Supervisor :	Dr. Wolfgang Löffler
Daily supervisor:	Drs. Thomas A. Steenbergen
Second corrector :	Dr. Michiel de Dood

Leiden, The Netherlands, January 16, 2026

The angle-dependent phase velocity of GHz acoustic waves in GaAs

Maja Wohlfarth

Huygens-Kamerlingh Onnes Laboratory, Leiden University
P.O. Box 9500, 2300 RA Leiden, The Netherlands

January 16, 2026

Abstract

Surface acoustic waves (SAWs) in gallium arsenide (GaAs) are promising carriers of quantum information and can couple to various quantum systems such as quantum dots. This coupling between acoustic waves and quantum dots can be enhanced using focused cavities. Due to the anisotropy of the acoustic wave velocity on GaAs, the mirror shape of focusing cavities needs to be adapted to the wavefront. In this project, we measure the angle-dependent phase velocity $\mathrm{v}(\theta)$ of acoustic wave modes in GaAs at GHz frequency, using a high-precision interferometric setup that captures the amplitude and phase of the acoustic displacement. To separate the acoustic modes by their spatial periodicities, we perform a spatial Fast Fourier transform (FFT) and extract the modes using ridge detection. We use the found spatial frequencies to calculate the angle dependent phase velocity. To our knowledge, this is the first study to combine full angle-resolved phase velocity measurements of surface and bulk modes simultaneously and the results show good agreement with the theoretical model.

Contents

Version of January 16, 2026– Created January 16, 2026 - 15:59

Chapter 1

Introduction

Surface acoustic waves (SAW), or Rayleigh waves, are elastic waves that are confined to the surface of a material. They decay exponentially into the bulk and are typically composed of a longitudinal and a transverse motion (see Figure 1.1) [2]. Acoustic waves propagate at phase velocities v that are four to five orders of magnitude smaller than electromagnetic waves. When considering frequencies f_t in the MHz to GHz range, we can conclude that acoustic wavelengths λ are rather small, since $v = \lambda \cdot f_t$. Hence, acoustic waves are more suitable for devices that are limited in space and make use of wireless communication, such as mobile phones [3–6]. A key application of SAWs is in RF filtering [3–6]. The filters can operate in frequency ranges from 0.4 to 2.2 GHz and have low insertion losses [3]*. With acoustic waves, multiple filters for varying regions and bands can be easily and cost-effectively integrated onto chips due to their small size, whereas the conventional electromagnetic microwave resonators barely meet the requirements for integration [3–6].
Acoustic waves are also used in sensing and mixing applications that are relevant in life sciences and microfluidics [4, 6, 7], for chemical sensing [6, 7], and for physical sensors and actuators [6]. With acoustic waves, one can manipulate fluids and small particles as, for instance, cells or bacteria. This is done with lab-on-a-chip devices that give us the option to perform operations as mixing or pumping tiny amounts of these fluids or particles [4, 7].

Furthermore, SAWs can couple to various two level systems such as quan-

*Bulk waves can also be used for filters, but they perform better at slightly higher frequencies.[3]

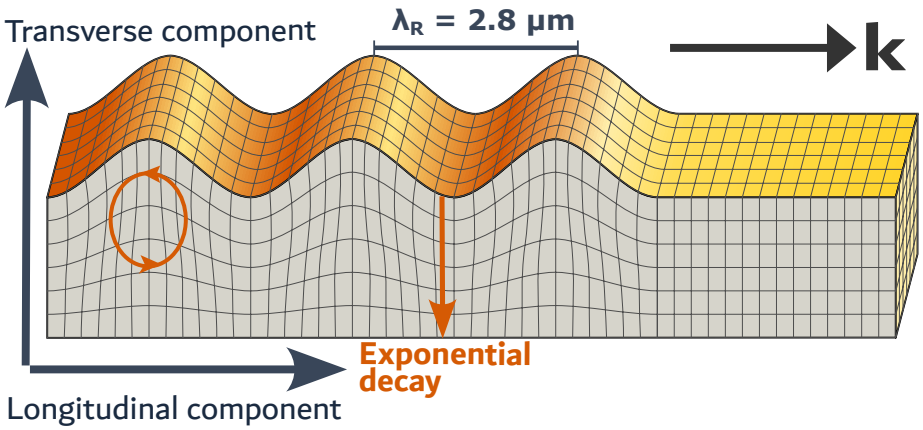

Figure 1.1: *Rayleigh wave. The wave travels to the right, in the direction of the wavevector* ***k*** *and displacements of atoms happen in the longitudinal and transverse out-of-plane direction. [1]*

tum dots (QDs), defect centers (e.g NV centers in diamond or divacancy defects in silicon carbide), trapped ions and superconducting qubits [4]. With this ability and the long coherence time of SAWs, they are suitable candidates for building quantum transducers that interface to multiple of those systems [4].

One of the most viable systems, or platforms, for quantum information processing are circuits at microwave frequencies that work with superconducting qubits [8]. However, when transferring information between distant circuits, qubits operating at microwave frequencies become susceptible to thermal noise in the ambient environment, which leads to decoherence [9, 10]. A better medium for quantum information transfer are photonic qubits in the optical range. With them, one can have low loss during transmission via fibers and the interaction with the environment is much weaker which decreases decoherence [11]. However, the corresponding frequencies for optical photons are in the high THz range and are about 10^5 times higher than in the microwave case. We therefore get a large mismatch between the frequencies, and a potential solution is to make use of an intermediate system. SAWs are able to do the microwave-to-optical conversion with low noise [4]. We can connect the superconducting with the acoustic system by using interdigital transducers (IDT). Their functioning is based on the inverse piezoelectric effect. To couple to the optical field, we can use InGaAs/GaAs quantum dots that are embedded in GaAs as is done in our group [12]. Those can produce single

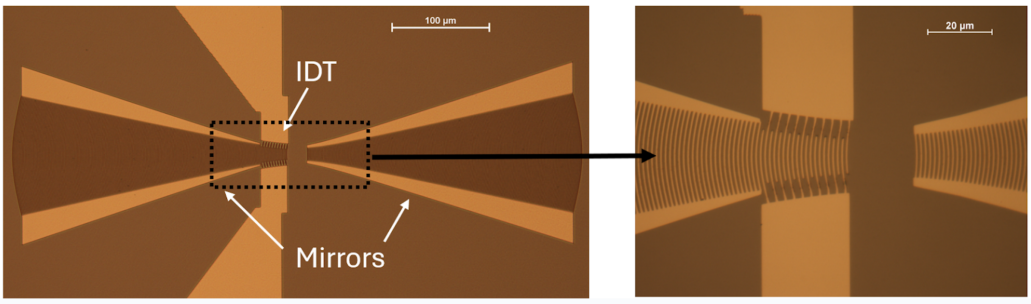

Figure 1.2: *Focused cavity. The two mirrors are acoustic Bragg reflectors and the interdigital transducer (IDT) with its interlaced fingers in the center creates the acoustic waves.*

photons when being excited by a laser. Acoustic waves can shift the quantum dot energy levels which can be detected through the emitted photon.

To obtain sufficient optomechanical coupling, the acoustic field should be strongly constrained around the QD region [4, 13, 14] and be close to the dimensions of the nanometer-sized structure [15]. This can be done by using focusing acoustic cavities with rounded mirrors [13, 15] (see also Figure 1.2). To obtain a small focus, one has to take into account the anisotropic properties of piezoelectric crystals such as GaAs in which SAWs travel [16]. The shape of the acoustic mirrors and the IDT has to be adapted to the wavefront shape, or the group velocity, as it carries the energy of the wave [15].

In previous research, the phase and group velocities of GaAs have been modeled by different approaches. One was to use quadratic approximations for small angles around the piezoelectric direction [16]. Another refined approach compared to quadratic approximations was to use numerical calculations to find the curve for constant frequencies, and the group velocity was modeled by a cosine [15]. However, this was limited to small angles around the piezoelectric axis and no analytic solution was shown. The approximations used as in Msall's paper [15] still appear to cause deviations of the measurement data from the model as shown in Young's double slit experiment on GaAs [17]. There have also been experimental approaches to measure the surface acoustic wave phase velocities at different angles as by Kuok who bases himself onto rigorous theory [18]. The study is restricted to an angle range of 45° which is in general sufficient due to the GaAs crystal structure, but the authors note a persistent phase velocity offset of 2.5 % or higher. To get a full experimentally validated theoretical model for acoustic waves in GaAs, one would need to perform

not only SAW, but also bulk wave measurements at varying angles.

In this project, we investigate the anisotropic properties of (001)-cut GaAs by measuring the angle-dependent phase velocities for bulk and surface acoustic wave modes with high precision. To achieve this, we use a sample designed to weakly scatter waves in all directions. We measure the amplitude and phase with an interferometric setup across the sample and perform a spatial Fourier transform. A ridge detection procedure is developed to extract the spatial frequencies from the data. This allows us to determine the angle-dependent phase velocities. Finally, these results are compared to a theoretical model.

The thesis is structured as follows. In Chapter 2 we introduce SAWs, explain how they can be created with IDTs and show briefly how the phase velocities for bulk and surface modes can be derived. In Chapter 3, we show the sample with scattering properties and the optical setup to measure the amplitude and phase of the acoustic displacement. We perform a spatial Fast Fourier transform and extract the frequencies in Chapter 4, derive the phase velocities in Chapter 5 and compare them to the theoretical model. A conclusion and outlook are given in Chapter 6.

Chapter 2

Theoretical Background

This chapter briefly introduces surface acoustic waves (SAW) with the associated displacement of atoms. Then, the GaAs crystal structure with relevant symmetries for our measurements on the (001) plane is explained. We give a brief background to the wave equations that describe the system and that can be solved to find the acoustic wave modes with associated phase velocities. The bulk modes are found by going via Christoffel's equation [2] and the surface modes can be found using Stroh's formalism [19]. Lastly, interdigital transducers are introduced to explain how SAWs are created.

2.1 SAWs and symmetries on (001)-cut GaAs

Before looking at how we can derive the phase velocities for wave modes in GaAs, it is of interest to get a basic idea of SAWs, or Rayleigh waves. Those can be decomposed into two components (cf. Figure 2.1). The longitudinal component describes the displacement of the particles in the direction of the wave propagation. The transverse component is directed out of the bulk and is normal to the surface. As they have a phase difference of $\frac{\pi}{2}$, the components cause an elliptical movement of the atoms in the material.

Furthermore, the wave components decay into the bulk, though not at the same rates, and are confined to the surface [2]. The displacements of the components are already strongly reduced at one SAW wavelength into the bulk. For instance, Figure 2.1b illustrates the decay of (010)-cut GaAs.

Understanding the crystal structure of gallium arsenide (GaAs) and the

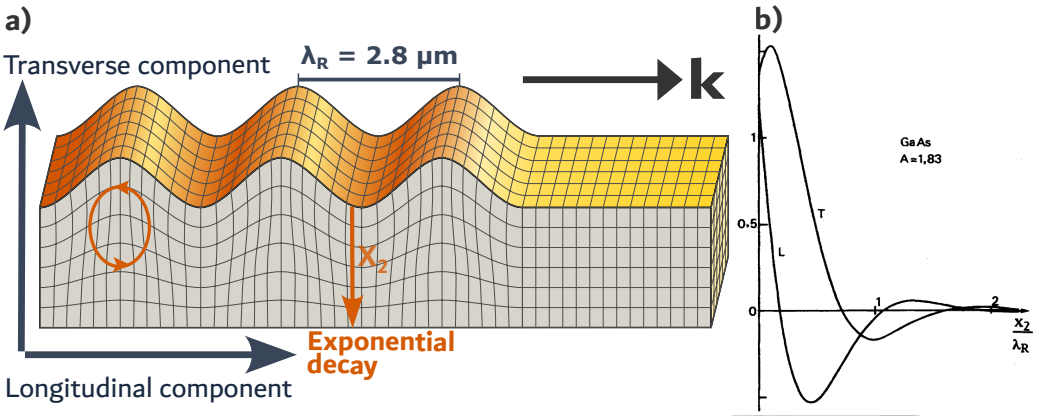

Figure 2.1: *a) Rayleigh wave. The transverse (T) and longitudinal (L) component add up to a elliptical movement of atoms and decay into the bulk. λ_R is the SAW wavelength in GaAs and* ***k*** *indicates the direction of propagation [1]. b) Change of displacement into the bulk of the SAW components in (010)-cut GaAs. x_2 is the distance into the bulk. A is the anisotropy factor as defined by Royer and Dieulesaint [2].*

symmetries connected to it can help us understand why wave modes such as the SAW mode change in phase velocity when looking at varying propagation directions.

GaAs has a zinc blende crystal structure (cf. Figure 2.2) that belongs to the $F\bar{4}3m$ space group. This means that type one atoms (i.e. Ga or As) are positioned at the corners and in the centers of the cube faces, as in a face-centered cubic structure. Type two atoms are then positioned at $\left(\frac{1}{4}, \frac{1}{4}, \frac{1}{4}\right)$, $\left(\frac{3}{4}, \frac{3}{4}, \frac{1}{4}\right)$, $\left(\frac{3}{4}, \frac{1}{4}, \frac{3}{4}\right)$ and $\left(\frac{1}{4}, \frac{3}{4}, \frac{3}{4}\right)$.

For our measurements, we take a (001)-cut sample. We are looking at the projections of the phase velocities and observe the symmetries belonging to this plane. In the projection, we have two mirror lines through the diagonals of the cube face, thus along [110] and $[\bar{1}10]$. These directions also happen to be our piezoelectric axes. The anisotropic structure of GaAs makes the piezoelectric interaction possible [20]. In addition, we observe a fourfold symmetry around the center of the (001) cube face. It follows that for every $90°$ we can observe the same pattern and in each quadrant there is a diagonal mirror axis. For our measurement, it means that it is enough, by crystal symmetry, to examine a sector of $45°$.

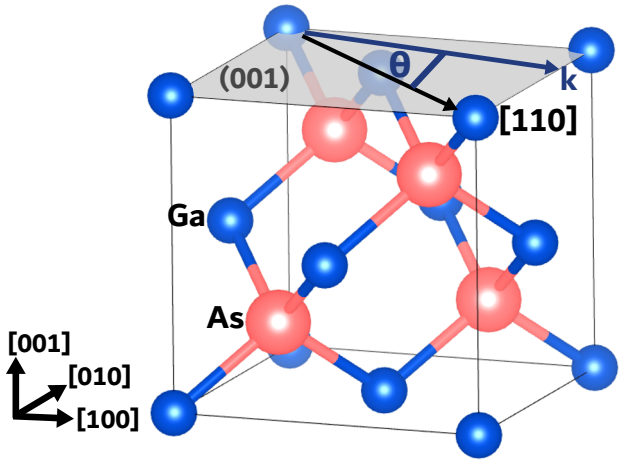

Figure 2.2: *The crystal structure of GaAs. The piezoelectric axis is along the* $[110]$ *direction. Our plane of interest for measurements,* (001)*, is colored light gray and the angle* θ *is measured as an angle from the piezoelectric axis to the propagation direction marked by the wavevector* $\boldsymbol{k}$*.*

2.2 Elastic Wave Modes in Gallium Arsenide

To develop an understanding of the particle movement and acoustic modes in GaAs, we start by introducing important quantities as stress and strain, explain how they are related, and introduce piezoelectricity. They can be used to find the wave equations [2]. We first show a sketch of the ansatz to solve them for bulk modes, and then for non-piezoelectric surface modes*. The solutions give us the phase velocities with their direction and displacement. The data of the angles and corresponding phase velocities of the theory (see figs. 2.3 and 2.4) is provided by Thomas Steenbergen of our research group who has developed a simulation of the surface and bulk wave modes.

We aim to understand the movement of atoms in GaAs thus we need to describe their motion relative to each other. Relative deformations can be defined by elastic strain and the restoring forces by stress. Stress and strain are linearly related via Hooke's law [2, 21]. The tensor relating the two is called the stiffness or elasticity tensor c_{ijkl}. We also need to define the stress

*For more elaborate explanations on the bulk wave derivation, I recommend reading [2, 21]. For the surface modes, Tanuma [22] covers the static and the piezoelectric case, but misses the dynamic, piezoelectric case, which is covered in [19].

at the surface of our material. For that, we define the traction

$$t_k = \lim_{dS \to 0} \frac{dF_k}{dS} n_k = T_{ik} n_i \quad , \tag{2.1}$$

where n_k is the surface normal, S the surface, F_k is the force that restores the deformed solid to its original shape, and T_{ik} the stress. The Einstein summation convention is used here and the indices $i = 1, 2, 3$ describe the three dimensions. The direction normal to the surface is for us the [001] direction and corresponds to the index 3.

As the $[110]$ axis of GaAs is piezoelectric, we need to take into account the coupling between electromagnetic and mechanical field. The direct piezoelectric effect arises when we apply stress to the material in one of the piezoelectric directions. This induces electric displacement, or a change in the polarization and electric field. There is also the inverse form of the piezoelectric effect. An applied electric field can cause the material to deform, which is crucial to understanding how we can create waves on GaAs [20] (see also section 2.3). Therefore, we need to introduce electromagnetic terms into the acoustic equations and mechanical terms into the electromagnetic equations. The latter can be derived from Maxwell's equations under the assumption that the electric field variations appear static when comparing them to variations in the mechanical field. For the mechanical equation, piezoelectricity is introduced via the stress and the electric field is related to it via the piezoelectric tensor e_{ijk}.
Finally, we obtain two coupled wave equations

$$c_{ijkl} \frac{\partial^2 u_l}{\partial x_j \partial x_k} + e_{kij} \frac{\partial^2 \Phi}{\partial x_k \partial x_j} = \rho \frac{\partial^2 u_i}{\partial t^2} \tag{2.2a}$$

$$-\epsilon_{jk} \frac{\partial^2 \Phi}{\partial x_j \partial x_k} + e_{jkl} \frac{\partial^2 u_l}{\partial x_j \partial x_k} = 0 \quad , \tag{2.2b}$$

where ϵ_{jk} is the dielectric tensor (or permittivity tensor), Φ the electric potential and x_k the position in space. The underlying assumptions include that there are no free charges and no acting volume forces. Note that the involved tensors can be reduced using the crystal symmetries and thermodynamic arguments [21].

2.2.1 Bulk Modes

First, we want to search for bulk modes and their phase velocities v. For that, we assume the material to extend infinitely in all directions. We denote the bulk spatial domain by $\Omega_{bulk} = \mathbb{R}^3$. In order to solve the equation

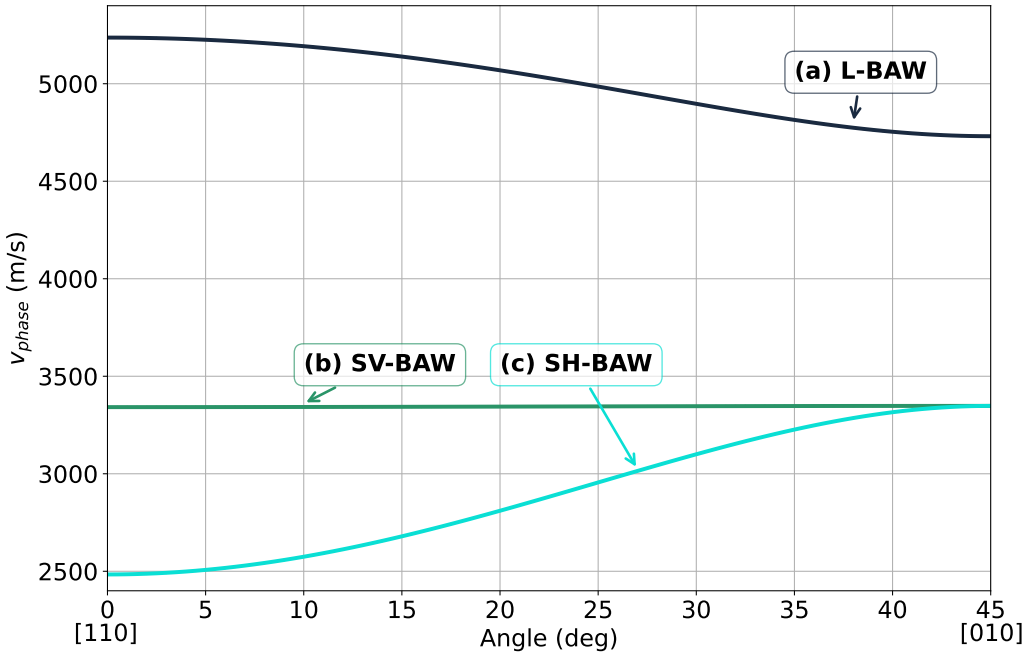

Figure 2.3: *Theoretical bulk phase velocities and their corresponding modes in the (001) plane of GaAs. (a) Longitudinal mode. (b) Shear vertical mode (Transverse, perpendicular to plane). (c) Shear horizontal mode (Transverse, in plane).*

system 2.2, a plane wave ansatz

$$u_i(x_j,t) = a_i e^{i[\omega t - k_j x_j]} \qquad \Phi(x_j,t) = \phi e^{i[\omega t - k_j x_j]} \tag{2.3}$$

can be used, where ω is the angular frequency, k_j the wave vector, a_i the displacement of atoms, and ϕ the displacement associated with the electric potential.

The term in the exponent can be rewritten as

$$\omega t - k_j x_j = \omega \left[t - \tfrac{1}{\omega} k_j x_j \right] = \omega \left[t - \tfrac{1}{\mathrm{v}} \hat{k}_j x_j \right]$$

with $\hat{k}_j = \frac{k_j}{k}$ a unit vector pointing in the direction of the wave vector k_j and the phase velocity v$= \frac{\omega}{k}$. We choose the wave vector to be in the (001) plane of the crystal (see Figure 2.2), which corresponds to our measurement plane. Therefore, the unit vector can be defined using $\hat{\vec{k}} = (\hat{k}_1, \hat{k}_2, 0)^T$. Using the [110] and $[\bar{1}10]$ directions as basis in the plane, we define the angle θ to be the angle between $\vec{k}$ and [110].

To solve the wave equations 2.2, one can insert the plane wave ansatz into them and rewrite them into into Christoffel's equation [2]. That is an eigenvalue problem, where the eigenvalues are the phase velocities and the eigenvectors indicate the displacement direction $\vec{a}$. Each solution corresponds to one mode.

There are three bulk modes, where one is (quasi-)longitudinal and two are (quasi-)transverse in their displacement (see Figure 2.3). The longitudinal mode can be characterized by a displacement in the direction of propagation. If the displacement of atoms is orthogonal to it, then we have a shear mode. There are the shear vertical and the shear horizontal mode, and they are orthogonal with respect to each other. The term "quasi" refers to the fact that the modes are not exactly longitudinal or transverse in our case, but there are small deviations. The displacement of the longitudinal mode $\vec{a}$ is not parallel to $\vec{k}$ and the shear modes are not exactly orthogonal to $\vec{k}$. In the [100], [110], [010] and $[\bar{1}10]$ direction the modes become pure modes, so $\vec{a} \| \vec{k}$ for the longitudinal mode [2, 21].

Due to the symmetries mentioned in section 2.1, it is sufficient to look at the angle dependent phase velocity $\mathrm{v}(\theta)$ in a 45° section (see figs. 2.3 and 2.4). We observe the three bulk modes, where the fastest phase velocity belongs to the (pseudo-)longitudinal mode. The two shear modes have the same velocity at $\theta = 45°$ which corresponds to the [100] or [010] propagation direction. We observe that the crystal structure actually looks the same in the two associated transverse displacement directions, which is not the case for other propagation directions.

2.2.2 Surface Modes

Let us recall the wave equations of Equation 2.2 and only take into account the case without piezoelectricity. The ansatz for surface modes needs to be modified such that it contains a decaying part into the bulk and the material boundary[†]. This means that we are only looking at a half-space $\Omega_{\text{surface}} = \{(x_1, x_2, x_3) \in \mathbb{R}^3 | x_3 \leq 0\}$ and we can further define the outward-pointing surface normal $\vec{n} = (0, 0, 1)^T$ along the [001] direction.

We follow the general approach as Tanuma [22]. Adding a decaying part $-\sqrt{-1}kpn_jx_j$ in the vertical [001] direction leads to

$$u_l(x_j, t) = a_l e^{-\sqrt{-1}k[-vt + m_j x_j + pn_j x_j]} \tag{2.4}$$

[†]Note that this part avoids using i for imaginary numbers and uses $\sqrt{-1}$ instead.

with $p \in \mathbb{C}$ and m_j being an in-plane unit vector, so $\vec{m} = (m_1, m_2, 0)^T$. The imaginary part of p indicates the amount of decay into the bulk. Only when $\mathrm{Im}(p) > 0$, we will get a decay [22].
As before, the ansatz is inserted into the wave equation. The idea is to go from a second order partial differential equation to a first order ordinary differential equation. We obtain Stroh's eigenrelation

$$N \begin{bmatrix} \vec{u^o} \\ \vec{l} \end{bmatrix} = p \begin{bmatrix} \vec{u^o} \\ \vec{l} \end{bmatrix} \quad , \tag{2.5}$$

where N is a real 6×6 matrix containing the information from the stiffness tensor, $\vec{u^o}$ is the displacement and $\vec{l}$ contains the traction, that needs to vanish at the surface of the material [22]. Here, it should be pointed out, that one surface mode is consisting of three partial waves of the form in Equation 2.4 that is a linear combination of three eigenvectors. The eigenvalues p come in complex conjugate pairs, so if three of them have an imaginary value $\mathrm{Im}(p) > 0$, then the other values $\mathrm{Im}(p) < 0$ [22].

The steps to obtain solutions are the following [‡]:
First, for a set angle, thus fixed $\vec{m}$, we vary the phase velocity from below the slowest bulk mode to above the fastest bulk mode. The Stroh matrix N can be calculated and we can solve the eigenrelation. This gives us varying sets of six eigenvectors and eigenvalues. The latter are sorted by their imaginary value. If three eigenvalues have $\mathrm{Im}(p) > 0$, then this could be a normal surface mode. If there are only two $\mathrm{Im}(p) > 0$, then it could be a pseudo surface mode. The third eigenvalue is selected to be the least growing one in terms of p ($\mathrm{Im}p = 0$). Then we check the boundary conditions set by the traction. The solutions with the phase velocity, that best fulfill our boundary conditions, are the chosen solutions[§]. Note that the $\mathrm{Im}(p) = 0$ eigenvector solution for the pseudo SAW resembles a bulk wave and is not decaying into the bulk.

It is also possible to extend the calculations to the case containing piezoelectricity. There would be a second equation for the ansatz and, after some substitutions and re-writing, the Stroh eigenrelation can be obtained for the piezoelectric case. The resulting problem is eight-dimensional. $\vec{u^o}$ now contains a fourth element, the electric potential, and $\vec{l}$ contains the electric displacement [19]. The results for the theoretical calculations for the piezoelectric case can be seen in Figure 2.4.

[‡]The theory is based on the work by Thomas Steenbergen.

[§]Note that one has to choose a cutoff of how good the boundary conditions on the traction are supposed to be fulfilled.

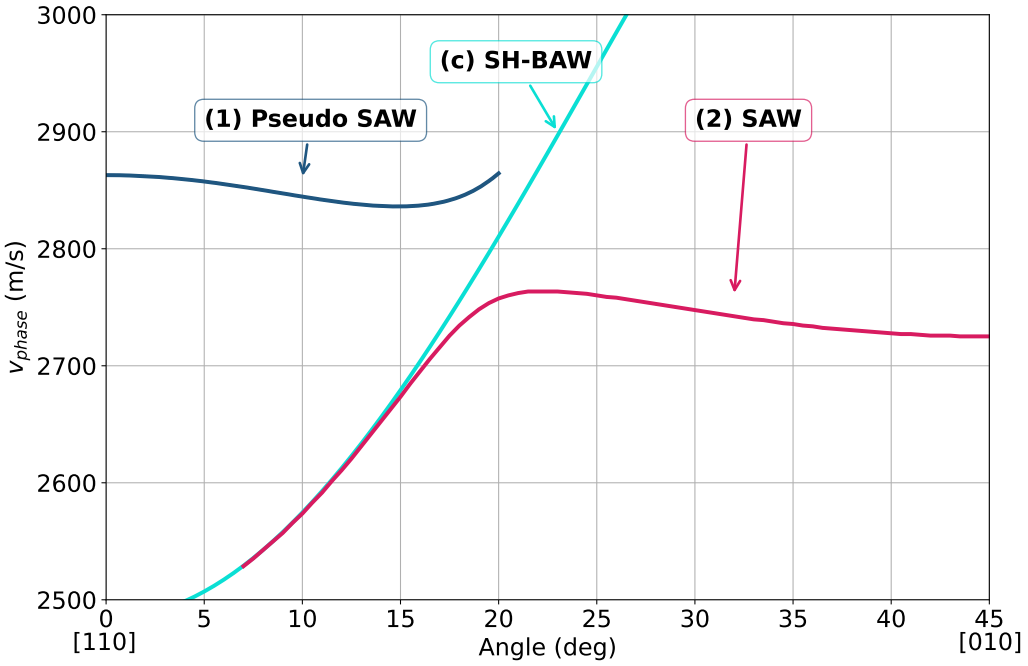

Figure 2.4: *Theoretical phase velocities and their corresponding modes in the (001) plane of GaAs. (c) Shear horizontal BAW.*

There are two major observations, which one can see in the figure. We observe an overlapping part between the pseudo SAW and the pure SAW mode, which resembles an avoided crossing, where the slowest bulk phase velocity line of the shear horizontal bulk mode crosses through the center of the avoided crossing. The pure SAW mode appears around the piezoelectric direction and the pseudo SAW mode at higher angles. The former always has a lower phase velocity than the bulk modes. Only when then bulk increases in velocity, the pseudo SAW starts to appear with a higher velocity.

2.3 Interdigital Transducers for SAW Generation

To create acoustic waves in our sample, we use the piezoelectric [110] axis (see Figure 2.2). That is the direction of pseudo SAWs (see Figure 2.4).

To excite acoustic waves the approach is to use interdigital transducers (IDT) that possess a structure similar to interlocking combs (see Figure 2.5a). We ground one comb and apply an alternating voltage to the other such

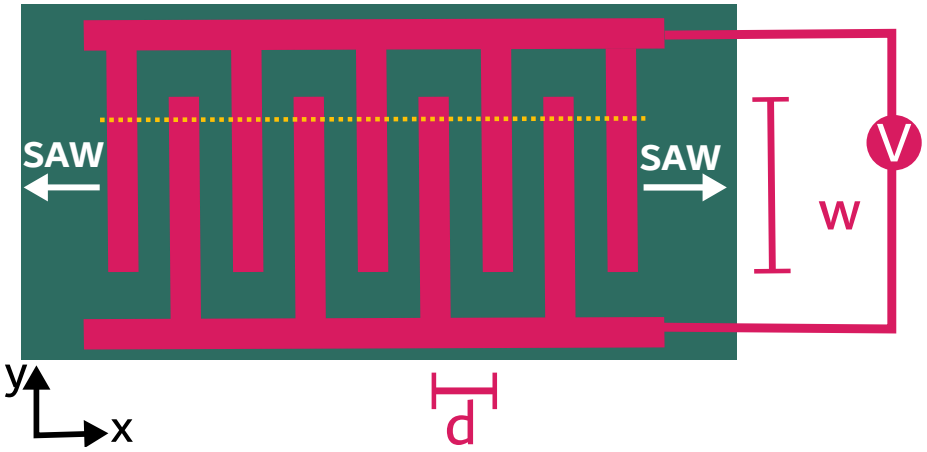

(a) *Top view of IDT. w: acoustic aperture, d: spacing between comb fingers. The dashed yellow line indicates where the cross section below comes from.*

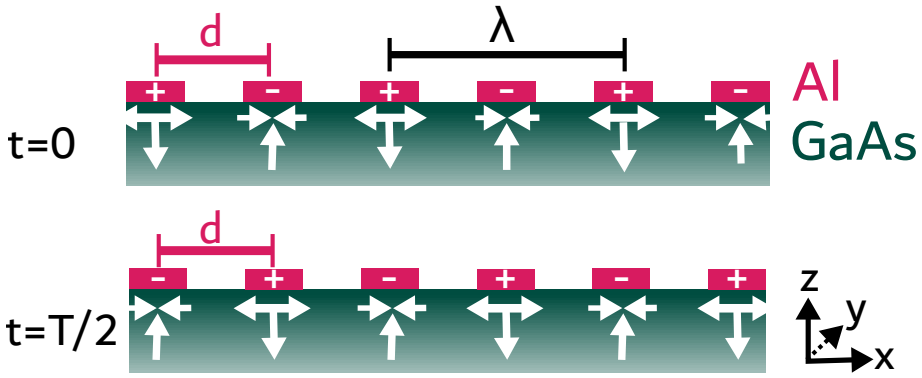

(b) *Cross section of IDT (see dashed yellow line above). Green: GaAs substrate where the waves travel. Pink: Aluminum electrodes for applying the voltage.*

that we get an electric field with alternating sign between neighboring comb fingers. Depending on the sign of the voltage, the inverse piezoelectric effect causes a deformation below a finger that consists of stretching or compression (see Figure 2.5b).

The compressions created under an IDT finger travel with the phase velocity v towards its neighboring fingers. The idea is to switch the polarity of the voltage when the deformation reaches the next finger so that it is amplified and we get constructive interference. To do so, the distance d between two neighboring fingers and the applied AC frequency f_t are of relevance. We set $d = \frac{\lambda}{2}$ and therefore the deformation reaches the next finger after $\frac{T}{2} = \frac{d}{v}$ corresponding to a frequency of the surface wave

$f_{SAW} = \frac{1}{T} = \frac{v}{2d}$. As mentioned above, the coupling occurs on the piezoelectric axis where pseudo SAWs are created. Given that we want to excite the waves efficiently at a frequency around 1 GHz and a phase velocity around 2800 ms^{-1}, we set the periodicity of the IDT fingers to $\lambda = 2.8\ \mu m$ [23].

Chapter 3

Experimental Methods

3.1 Sample design

The sample for this project is shown in Figure 3.1 and primarily consists of (001)-cut GaAs. An IDT has been patterned at the center of the sample's surface to generate acoustic waves along the [110] piezoelectric axis. The IDT fingers are located within the black rectangular region and are connected to the two parts above and below. A zoomed-in view reveals their comb-like structure. To observe the omnidirectional propagation of acoustic waves, we require scattering and reflection of the waves. Two areas to the left and right of the IDT are patterned with 1 μm metallic dots in a random arrangement, designed to weakly scatter the waves (see zoom-in). The sample has been fabricated using a lift-off process with electron-beam lithography (EBL). GaAs serves as the substrate for IDT and scattering areas, that consist of layers of titanium (3 nm), aluminum (44 nm) and titanium (3 nm). The metals have been deposited using evaporation.

While this thesis focuses on the phase velocity of the omnidirectional acoustic waves, one could also investigate the scattering areas themselves. For example, by measuring amplitude and phase, one could gain insights into the localization of waves within the random media created by the design.

3.2 Setup

We measure the acoustic amplitude and phase with an optical interferometric setup (see Figure 3.2) that is described in great detail by Fisicaro et

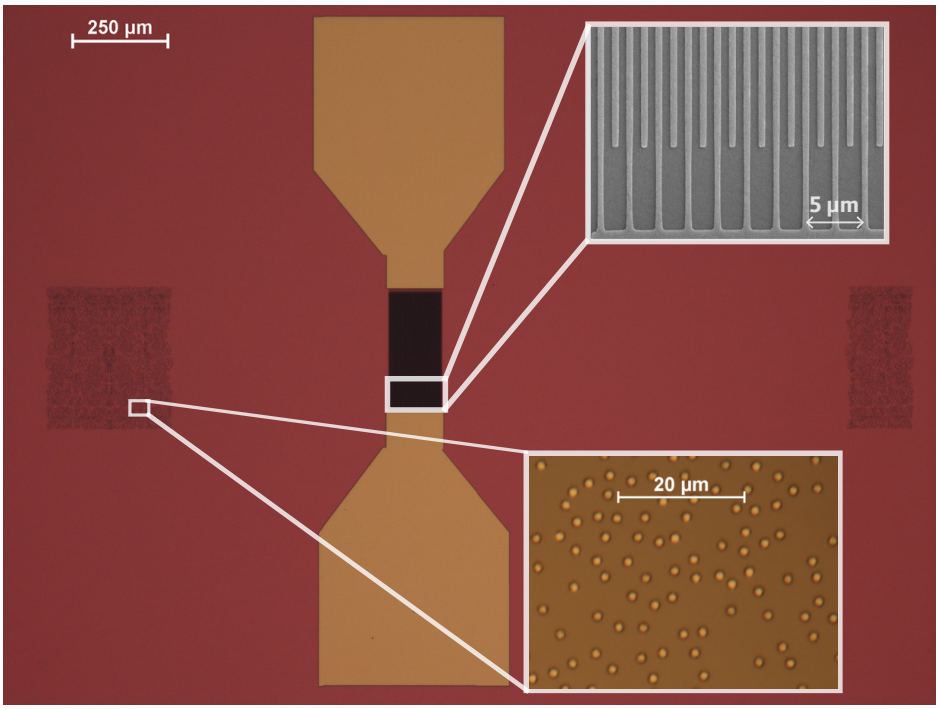

Figure 3.1: *Sample with IDT (center) and two scattering areas. Zoom-ins reveal the structure of the IDT fingers and the scattering area.*

al. [24].

Before a measurement can be started, we need to make sure that acoustic waves are created by driving the IDT on the sample with a RF generator. Then, coming from source A, 980 nm continuous laser light is passed through a 50:50 fiber polarization maintaining beam splitter (PM BS) into the sample (D) and reference (C) arm of a Michelson interferometer. Once in the sample arm, the light travels through free space, where it is collimated and focused perpendicularly onto a spot (diameter $\approx$ 2.8 μm) on our sample surface using two lenses. We scan over the sample by moving the stage onto which the sample is mounted and the displacement out of plane on the sample causes changes in the optical path length (OPL) of the sample arm. The light in the reference arm is reflected back by a mirror mounted onto a piezo. The reflected light from both arms travels back through the 50:50 beam splitter where it interferes and travels to another 30:70 beam splitter. The larger part of the interferometric signal is read out with a RF photodiode (RF PD).

The optical power fluctuations measured with the RF PD are inserted into

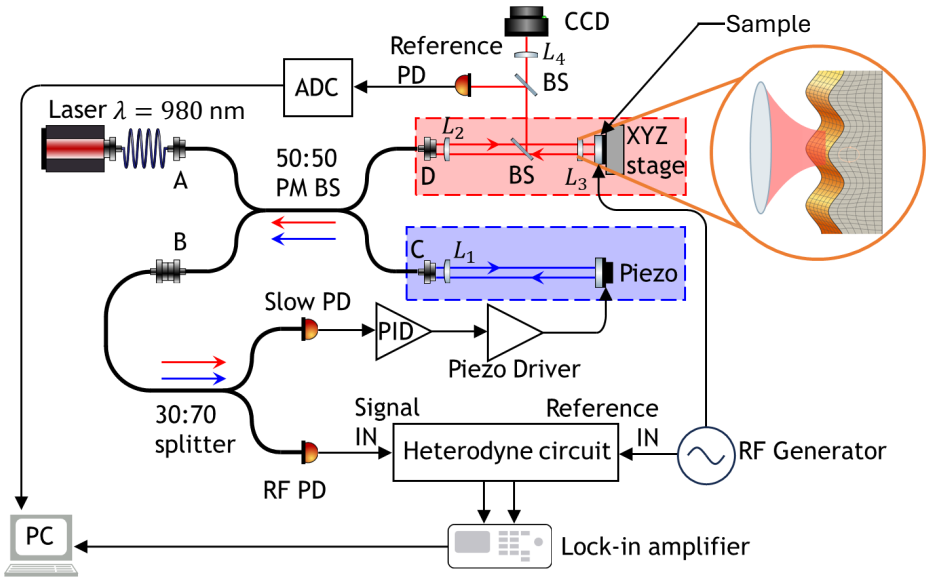

Figure 3.2: *Setup. Michelson interferometer with input laser (A), sample arm (D), reference arm with piezo (C) and output via (B). Slow PD for feedback to reference arm and RF PD for measurement signal itself. The RF generator creates a signal for the sample IDT and the heterodyne circuit. The full wave information (i.e. amplitude and phase) is recovered with the lock-in amplifier.*

the heterodyne circuit. A fraction of the original RF generator signal is split off and directly inserted through another port into the heterodyne circuit to serve as a reference.
We need to first down-convert the signals from GHz to MHz frequencies (here 22.05 MHz) with a local oscillator. Note that the heterodyne circuit only detects the time average of our fluctuations (i.e. root mean square power values) at every pixel. Only at lower frequencies can we demodulate the measurement signal with a lock-in amplifier to obtain amplitude and phase of our acoustic waves. The reference signal serves as external oscillator.

The portion of the light that does not enter the RF PD is read out with a slow photodiode (slow PD). The signal from the slow PD serves as error signal, which is used to lock the system at the side of the fringe. A proportional-integral-derivative (PID) controller, along with an amplifier and piezo driver, then provides feedback to drive the piezo and stabilize the interferometer.

In the sample arm of the interferometer, a part of the light can be directed to either a CCD (charge-coupled device) camera to navigate over the sam-

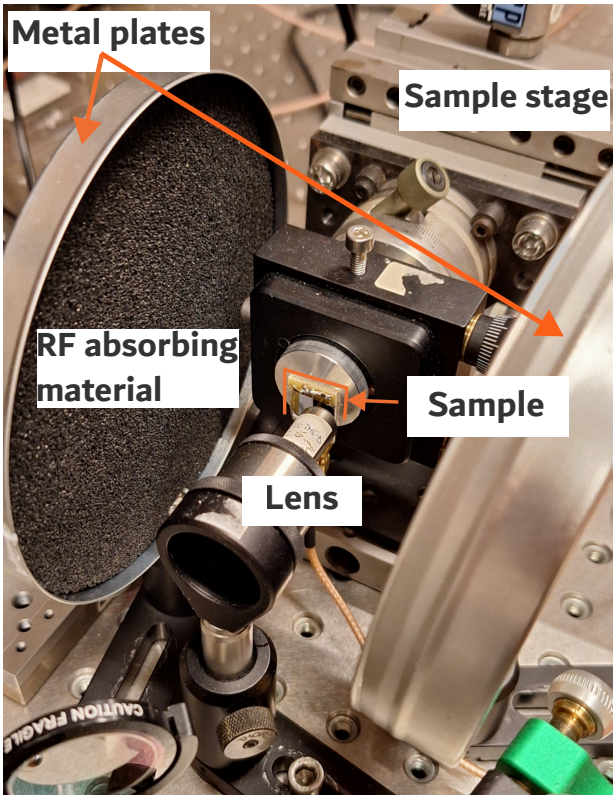

Figure 3.3: *Picture of sample mounted on sample stage and plates to the sides to reduce RF leakage. A lens in front focuses the incoming laser light onto the sample.*

ple and to adjust the laser focus, or to a reference PD that is combined with an analog-to-digital converter to record the reflected DC power during measurements.

Figure 3.3 shows the lens that focuses the light on the sample which is mounted onto a sample stage. The stage can move in 14 nm steps in the horizontal direction and in the vertical direction the step size depends on the settings on scanning area, scanning speed and amount of scanned lines. Note the two round metal plates that are filled with RF absorbing material to the sides of the sample and lens. During measurements, one can observe RF leakage that is originating from the sample or the connected cable carrying the RF signal. The RF measuring electronics take up the leakage signal. We try to reduce this by encasing the RF PD into a metal box and covering the signal-carrying cables with metal mesh and aluminum foil. The two plates with RF absorbing material are helpful in

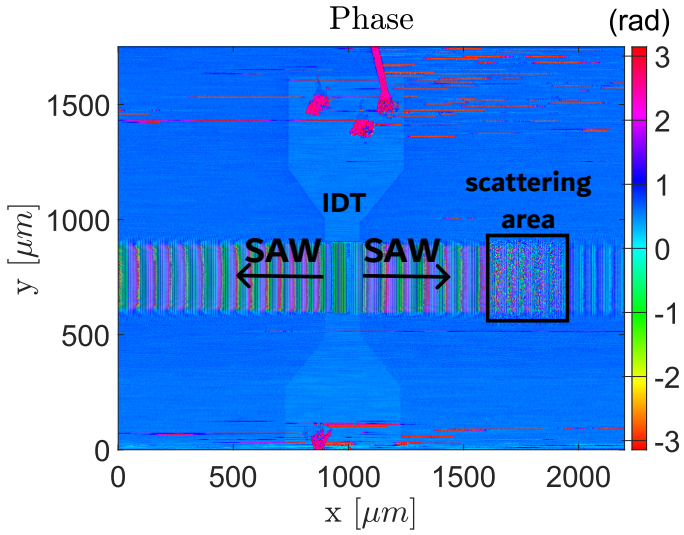

Figure 3.4: *Phase measurement at the IDT and scattering area to the right. Arrows indicate the waves created by the IDT. (measurement 04)*

further reducing the noise in the measured signal.
There also exist different measurement approaches to deal with RF leakage such as intensity-modulated spectral interferometry that down-convert the signal before measuring to be able to do measurements at lower frequencies with a spectrometer [25]. A second approach is to apply a voltage from two sides to the IDT with a π phase shift. This is shown in the paper of Ota et al. for a scheme with 3 GHz frequency [26]. The corresponding electromagnetic wavelengths around 100 mm are much larger than the size of the IDT ($<$ 1 mm) and the electromagnetic fields at the pads can destructively interfere. That leads to a great reduction of around 90 % of the electromagnetic field in the surrounding [26].

3.3 Measurement of amplitude and phase

To get an idea of typical measurements, we can briefly look at the phase measurement that includes the IDT and one of the scattering areas. In Figure 3.4, we observe waves created by the IDT that are traveling in the horizontal direction to the right and left. The waves coming from the IDT are indicated by arrows. Due to the low resolution in this figure, we take

Figure 3.5 to characterize the phase in detail. The IDT is clearly visible, and with it the pink dots related to the wire bonding. The horizontal pink stripes that are mostly at the top and bottom can be related to moments when the interferometer was not locked.

Our main area of interest (see Figure 3.5e) comprises the free GaAs next to the IDT together with the smaller scattering area, which lies on the same side of the IDT. The waves travel mainly from the right to the left.
On Figure 3.5a we can observe the amplitude. The SAW amplitude appears as a broad, uniform band propagating away from the IDT. It is the highest for the largest and the lowest for the smallest x values inside the band. There are highly localized spots in the scattering area. We also note weakly visible lines emerging up- and downwards from the scattering area. From the behavior of the amplitude, we can already see that there is only weak scattering effects visible and large parts of our waves are being transmitted.
To understand how much waves are transmitted, we consider the average of 10 amplitude cross sections between y = [550 μm, 750 μm] (see Figure 3.5c). The amplitude close to the IDT is around 0.13 mV and we observe a slight decrease in the negative x-direction until the scattering area is reached around x = 500 μm. At x-values corresponding to the scattering area, we observe narrow peaks, the largest with a 0.23 mV amplitude. There is an overall decrease in amplitude and after the scatterers the amplitude is around 0.08 mV that is approximately 38 % smaller than next to the IDT. More than 60 % of the waves have been transmitted.
The phase (see Figure 3.5b) can be better understood by looking at a cross section of the wave created by the IDT. We observe a sawtooth shape on the cross section part (see Figure 3.5c) that corresponds to free GaAs. It means that the phase is linearly in- or decreasing. At the scattering area, there are phase jumps. After that, the periodic sawtooth pattern is visible again. Coming back to the full phase plot in Figure 3.5b, we observe the phase jumps all over the scattering area and a complex pattern above and below the area that indicates the existence of waves in many directions. Note that the phase encodes the periodicity of the waves.

To improve our understanding of the scattering effect of our scatterers, we can zoom in on one of the scattering areas. One of the scattering dots can be seen in Figure A.1 of section A.1.

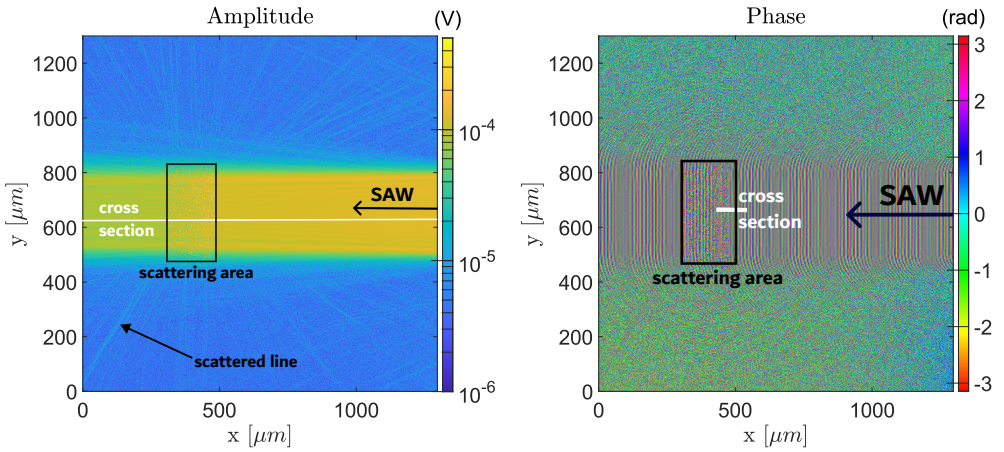

(a) *Amplitude.* **(b)** *Phase.*

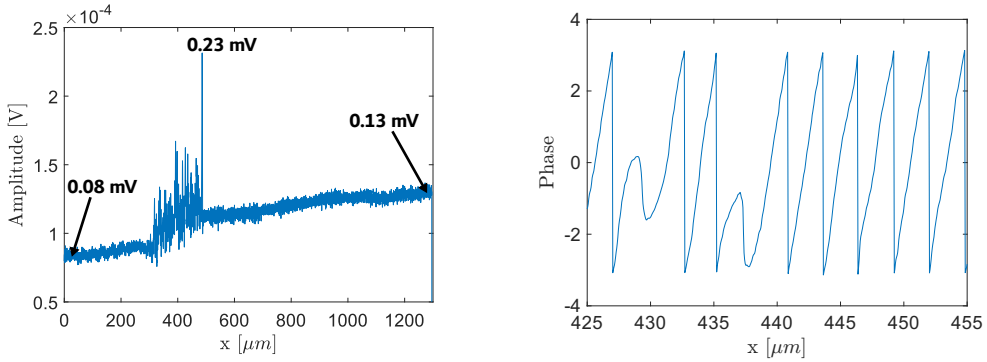

(c) *Amplitude cross section at y=650 µm* **(d)** *Phase cross section at y=650 µm*

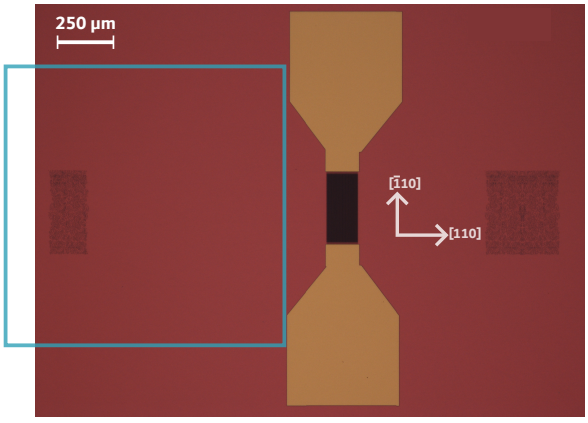

(e) *Figure of sample. The measurement area is indicated by the square box.*

Figure 3.5: *Measurement used for data extraction. (a) shows the amplitude with a cross section made visible in (c). (b) shows the phase with a cross section (d). (e) shows the chosen area for the measurement on the sample. (measurement 33)*

Chapter 4

Spatial Fourier Analysis

Our goal is to identify acoustic modes from the experimental scans. For this, we first use the amplitude and phase to find the spatial frequencies of the measured acoustic waves. In the next step, we calculate the phase velocity v with the associated angle θ from the frequencies. The modes are then identified using the theoretical model in the chapter that follows.

We take the amplitude and phase from the measurement as in Figure 3.5 that covered a region that included the smaller scattering region. Amplitude A and phase ϕ contain the full wave information, $A \cdot e^{i\phi}$. To find the spatial frequencies, we make use of a 2D Fast Fourier transform (FFT). Although we want to use an area that is as large as possible for our evaluation, we cannot use the scattering region to find all the wave modes. Using the scattering region means adding noise to our frequency picture. However, we want to still keep the apparent resolution large, so we choose to pad the region with zeros (see Figure 4.1). With that, the frequency bins will stay finer, and it is easier to distinguish peaks. Before we can perform the FFT, we apply a window to the region next to the region that has been padded with zeros. This can be done to reduce spectral leakage that arises due to the limited measurement space. We typically use a circular Kaiser window because we want to measure waves with high precision in all directions, but it is also possible to use a rectangular Tukey (or cosine-tapered) or Kaiser window in general.

Using MATLAB, we then perform the FFT to extract the spatial frequency information. As the resulting values of the FFT are complex, we look at their magnitude which shows us the strength of different spatial frequen-

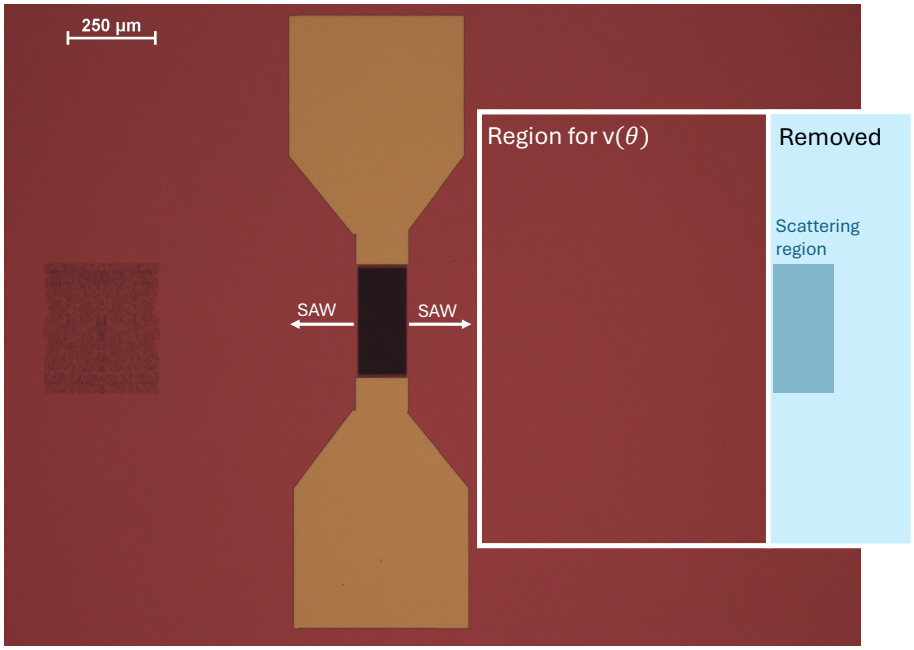

Figure 4.1: *Sample with marked measurement region. It is split into the removed region that is padded with zeros and the region on which the window is applied. The scattering regions is marked inside the removed region.*

cies. We call the high-magnitude regions ridges as they mostly come as long lines. Figure 4.2 shows a typical FFT obtained after measurements with our sample. Note that there is a trade-off for the strength of the window, that is, for how fast values decrease. A stronger window might reduce the spectral leakage that is caused by the FFT, but simultaneously spectral broadening is happening where lines in the FFT get broader. The latter effect can make smaller features less visible. The data is saved for further use in a H5 file.

As expected from the theory on crystal structure in section 2.1, the FFT plot (see Figure 4.2) has an overall 4-fold symmetry and four mirror axes that are vertical, horizontal and diagonal, when considering the circular lines. In principle, it would therefore be enough to discuss one octant. For more complete data points for each mode and for a simplification of the results, we choose to combine data from the four quadrants by using the horizontal and vertical mirror axes. We fold the data into one single quadrant by choice. As our sampling in x and y can be different depending on the measurement, we choose not to use an octant, because methods, as interpolation, would be required for the folding. Further, the ridge detection

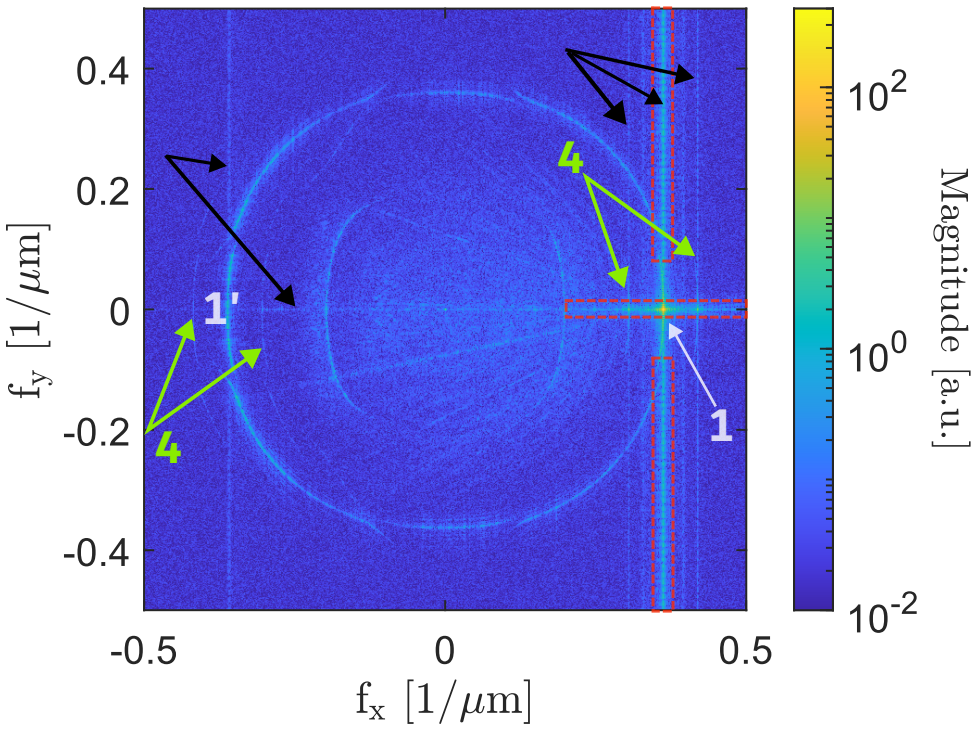

Figure 4.2: *FFT plot from measurement between IDT and small scattering region. Red rectangles with dashed lines mark where the pixels have later have been modified. The strongest magnitude region is around (1), followed by (1'). Black arrows point at spectral leakage lines. Green arrows point out the sidebands.*

of the data extraction method, that is explained at the end of this chapter, would not work as well having a diagonal border line of the octant. It is of course also possible to skip the folding and to consider at all spatial directions.
We further attribute the straight lines that break the symmetry to spectral leakage effects. We observe vertical and horizontal lines going through the regions of strongest magnitude in the FFT, so around (1) and (1'). It is not clear why they are mainly visible in vertical and horizontal directions despite having used a circular window before taking the FFT. It might be related to the underlying image being rectangular and divided into rectangular pixels. We can also observe diagonal lines emerging from the region of strongest magnitude, where one is particularly well visible. This could also be due to spectral leakage.

In addition, we observe parallel lines to the right and left of the highest

magnitude regions (see Figure 4.2, (4)). They bear resemblance to sidebands. When looking closely, we can even see gaps as in the central line between the sidebands, but shifted in x direction. Their origin lies probably in the periodicity of the stage motor in x direction. The motor ends one turn after approximately 15 μm which corresponds to a frequency of approximately 0.6 μm^{-1}. The sidebands in the FFT are also approximately 0.6 μm^{-1} away from the surface mode lines, and we only observe the shift in x direction. We suggest therefore that an amplitude modulation, that is related to the x direction stage motor, might cause the sidebands. Similarly as in the highest magnitude regions, we can see perfectly straight vertical lines emerging from the upper and lower ends of the sidebands that originate from the spectral leakage.

The visible modes at higher angles are better visible on the left side of Figure 4.2, which could be related to them being created by the scattering centers and edges of the sample that cause backscattered waves. This leads to a wider angular spread of propagating waves and less concentration to the [110] crystal direction (labeled as main propagation axis). We label the waves as forward traveling on the right side of our FFT and as backward traveling on the left side.

Before being able to extract the spatial frequencies that correspond to our ridges in the FFT, we need to consider the spectral leakage lines with the highest magnitude marked with red rectangles in Figure 4.2. If we do not deal with them, they are detected during the later ridge detection. For the vertical line, we only consider the parts above and below the high magnitude region. We choose a width in x and replace inside values of the line with averaged magnitude values from a few pixels to the left and right outside the region. The horizontal line segment is dealt with in a similar manner. In this case, pixels above and below the line are taken for replacement.

The process of extracting spatial frequency data from the FFT plots and to obtain from it $v(\theta)$ is illustrated in the flow chart in Figure 4.4 and is done in Python. The FFT returns a complex number for every spatial frequency coordinate (f_x,f_y) where the highest detected frequencies are limited by the resolution in real space, or by the sampling rate. We want to know how strong frequencies are in our measurement. Therefore, we consider the magnitude of the Fourier transform. As there are only few strong signals and a lot much weaker signals, we need to improve the detectability of weak against strong lines. For that, we first normalize the data and then apply a log-scaling. Then we use Gaussian smoothing to suppress small

structures related to noise and get a scale-space representation that is used for further steps. The scaling has to be specified by the σ parameter which represents the standard deviation of the Gaussian kernel. It is included in the functions for line, or ridge, detection.

The following ridge detection is then done with filters of the scikit-image library* which are based on the Hessian matrix

$$\mathbf{H}_L = \begin{pmatrix} \frac{\partial^2 L}{(\partial \mathrm{f_x})^2} & \frac{\partial^2 L}{\partial \mathrm{f_x} \partial \mathrm{f_y}} \\ \frac{\partial^2 L}{\partial \mathrm{f_y} \partial \mathrm{f_x}} & \frac{\partial^2 L}{(\partial \mathrm{f_y})^2} \end{pmatrix} \tag{4.1}$$

that describes the local curvature of a function L, in this case, the magnitude in the scale-space.

We have tried the filters based on methods by Frangi [27], Meijering [28] and Sato [28]. Frangi's method has worked the best, but Meijering might be a good alternative. Sato was sorted out due to much background noise being picked up.
Figure 4.3 shows an example of the ridge detection with Frangi's filter and the steps we performed afterwards. The output of the ridge detection is the ridge-ness score r which is a measure for the ridge strength and assigned to every pixel on the grid. A higher value is obtained for pixel areas with higher magnitude. Depending on the exact method it can be referred to as the vesselness (Frangi) or the neuritness (Meijering). The result is binarized by setting a threshold to the ridge-ness score. This can filter some of the background noise, that has been erroneously detected and leaves us with the detected ridges.

To identify the different modes, we use DBSCAN clustering of the scikit-learn library†. Important parameters for the clustering are `eps`, the distance within points are considered as neighbors, and `min_samples`, the minimal number of points in the neighborhood to consider a point a core point. The larger `min_samples`, the denser clusters found will be. In case some noise has been clustered, it can be sometimes filtered out by only taking clusters with a smaller or larger amount of points. Finally, we get a list of frequencies for each cluster that correspond to different modes in the optimal case.

The just introduced extraction steps bring a few challenges. One wants to keep ridges that actually belong to lines and discard noisy data points

*`https://scikit-image.org/docs/stable/api/skimage.filters.html`
†`https://scikit-learn.org/stable/modules/generated/sklearn.cluster.DBSCAN.html`

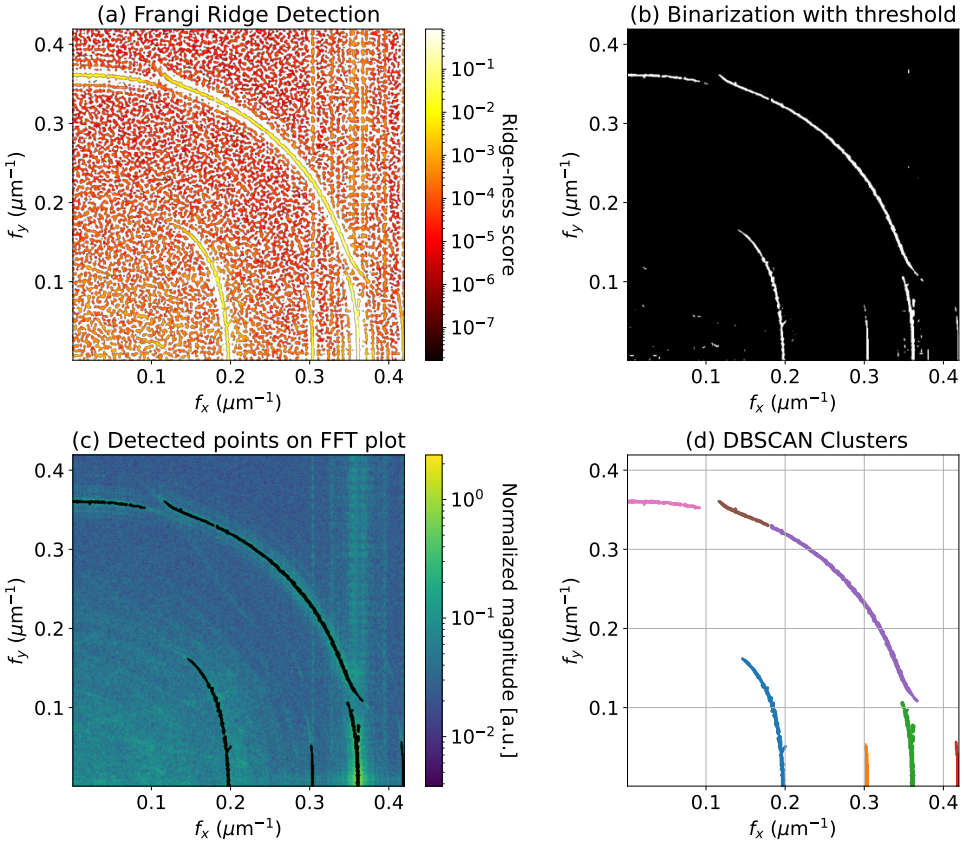

Figure 4.3: *Steps to extract points in lines. (a) Ridge-ness score r(f_x,f_y) after Frangi ridge detection. (b) Binarization of the data for r > threshold (white = True, black = False). (c) Detected points in black shown on FFT plot. (d) Found clusters via DBSCAN clustering.*

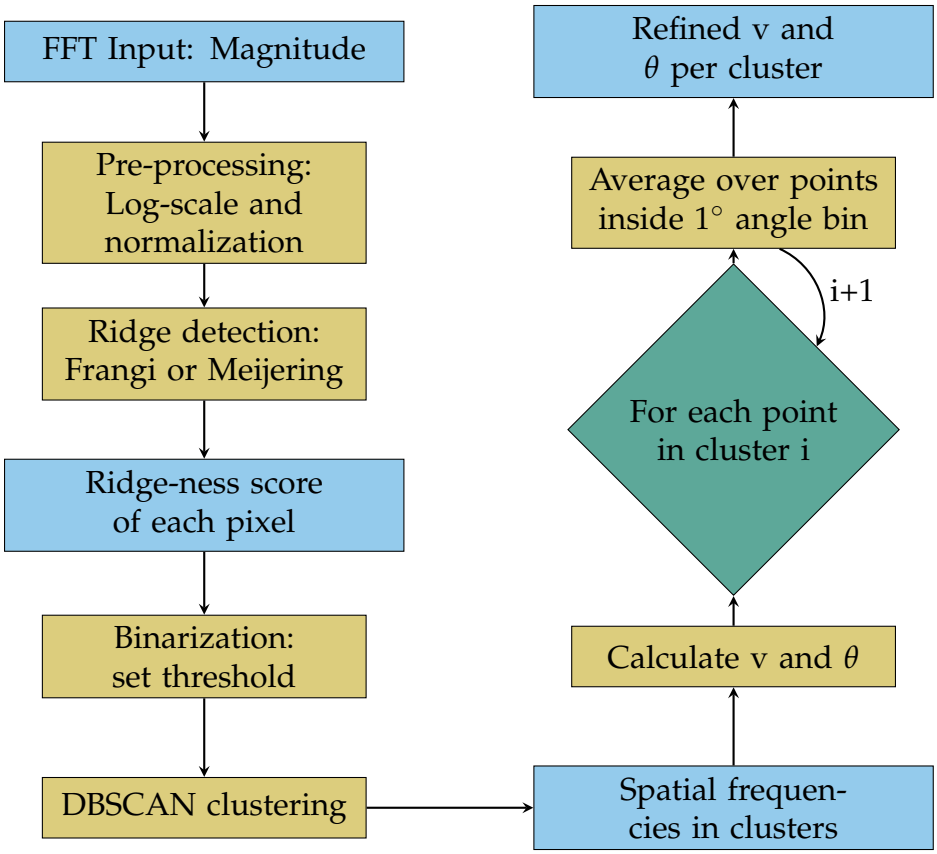

Figure 4.4: *Flowchart illustrating the data extractions steps from the FFT to the refined values for v and θ.*

and artifact lines. Even with the normalization and log-scaling, some relevant lines that are visible by eye have a magnitude at the order of noise in other regions. This makes it hard to detect those weak lines. Either there are methods through the measurement technique and sample design to reduce further noise, or one can also restrict the area on which ridge detection is performed. For detecting the shear vertical bulk mode it has been helpful to zoom into a rectangular area around the line. As it was only visible on the left half-sphere, only the two left quadrants have been combined instead of taking all. The Python code is split into two files that permit us to extract the frequencies and then calculate $\mathrm{v}(\theta)$. Therefore, it is possible to do the general ridge detection where all quadrants are combined and then detect, for instance, a low magnitude line of the chosen region. Two obtained frequency files for the full and only the weak line region (in H5 file format) can then be used in the next step.

The extracted spatial frequencies $\mathrm{f_x}$ and $\mathrm{f_y}$ with their associated magnitude m can be used to calculate the associated angle θ and phase velocity v by

$$\theta_i = \arctan \frac{\mathrm{f_{y_i}}}{\mathrm{f_{x_i}}} \tag{4.2}$$

$$\mathrm{v}_i = \frac{\mathrm{f_t}}{\sqrt{\mathrm{f_{x_i}^2} + \mathrm{f_{y_i}^2}}} \quad , \tag{4.3}$$

where $\mathrm{f_t} = 1.03205$ GHz is the temporal frequency of the waves. Recall from section 3.2 that $\mathrm{f_t}$ can be set via the function generator in the experimental setup. The zero degree angle is defined for $(1,0)^T$ in the coordinate system (corresponding to [110] crystal direction) and $(-1,0)^T$ represents $\pm 180^\circ$. The angles decrease in the clockwise direction and increase in the other direction. Subsequently, we divide the data into one-degree angle bins. For each bin, the weighted average of angles and phase velocities is calculated by $\bar{\theta} = \frac{\sum \mathrm{m}_i \cdot \theta_i}{\sum \mathrm{m}_i}$ (idem for v).

Version of January 16, 2026– Created January 16, 2026 - 15:59

Chapter 5

Results and Discussion on v(θ)

This chapter shows the results using angle-resolved phase velocity graphs and the FFT, compares them to the theoretical model and refers to what can be further seen on the FFT. Observations on the measured modes and deviations are discussed.

Figure 5.1 displays extracted values from one of our measurements with their associated variance in terms of the error due to the pixel size in our FFT plots and due to the averaging which gives a geometric error. Calculations for those can be found in the Appendix A.2.

We observe that the angle dependent velocities of the detected acoustic modes are in good agreement with the theoretical model. From the bulk modes (see (2a-c)), we managed to find the longitudinal mode (2a) around the [110] crystal direction up to 45°. The shear horizontal mode (2c) could only be detected at larger angles that are further away from the main propagating direction and the shear vertical mode (2b) has not been detected. Both surface modes have been found. For the pseudo SAW mode (1), only the last part at the avoided crossing has not been extracted. The SAW mode (3) results also agree well with the theory and there is a part of the pure SAW mode below the pseudo SAW mode that has not been found despite the boundary conditions still being fulfilled according to the model. We note that the sidebands, as pointed out in Figure 4.2, have been detected, too.

To gain deeper insight, we now discuss the origin and nature of the modes. Recall that we primarily generate pseudo SAWs on our sample, so we seek to understand why we observe other modes. Pseudo SAWs can couple to

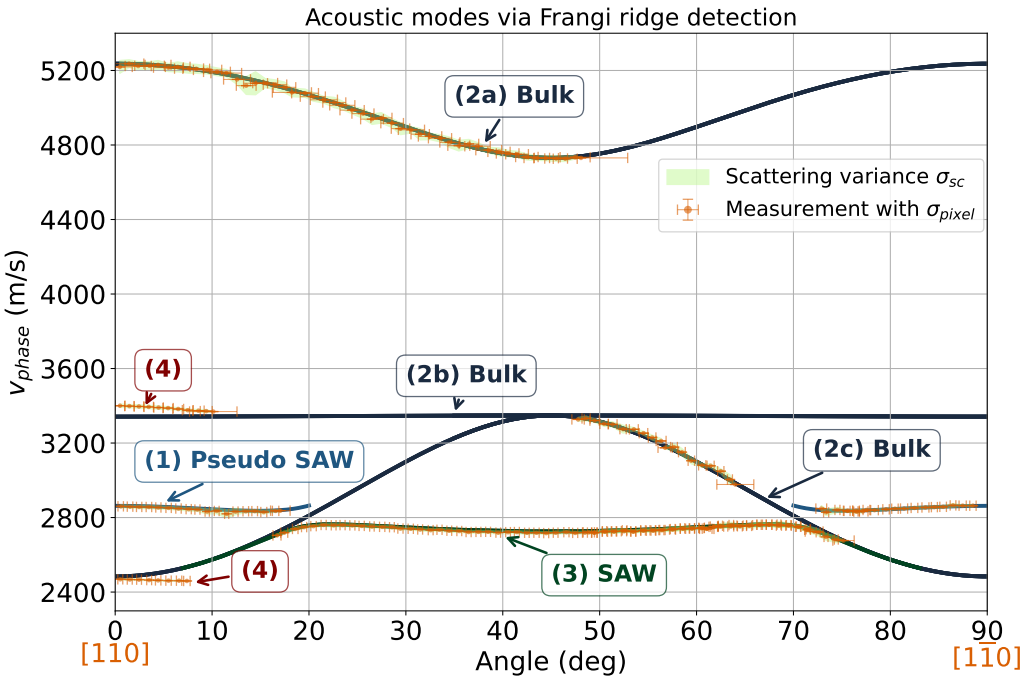

Figure 5.1: *$v(\theta)$ results for the (001) plane in GaAs. (1) Pseudo SAW, (2a) Longitudinal BAW, (2b) Shear vertical BAW, (2c) Shear horizontal BAW, (3) SAW, (4) Sidebands*

other modes, but we cannot say for sure what kind of coupling is happening in this measurement. Besides, surface modes can be scattered into bulk modes by the IDT, the scatterers and the sample edges. To understand why modes are excited, we would need to perform further analysis of our measurements. The fact that we can measure the longitudinal and the shear horizontal bulk mode at the surface might seem illogical as they are not expected to have out-of-plane components which change the optical pathlength. We have thought of two mechanism that could make it possible for us to measure the modes nevertheless. The first is that the refractive index of the surface is changed by the acoustic wave which changes the acousto-optic interaction during the reflection of light in the interferometer. The second is that the boundary conditions on traction can alter the displacement profile of the modes, possibly introducing an out-of-plane component at the surface of our sample.

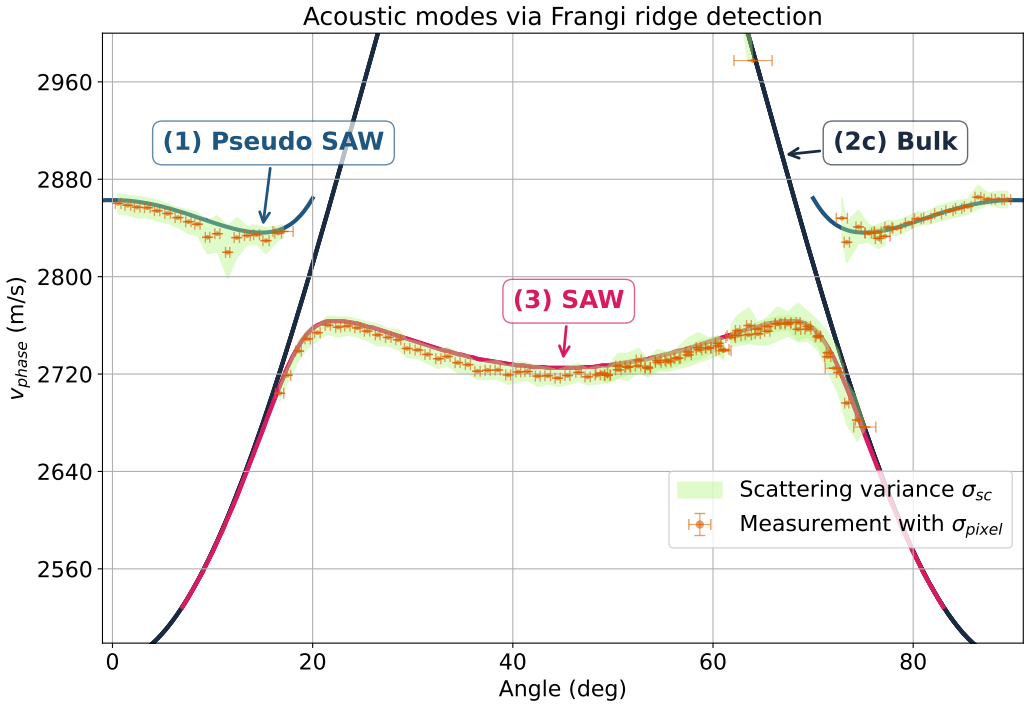

Figure 5.2: *$v(\theta)$ zoom-in. Mode anti-crossings involving the pseudo SAW and pure SAW mode. The shear horizontal bulk mode is passing through the centers of the avoided crossings according to the theoretical model.*

Avoided crossings of modes

We can also have a closer look at the part, where both surface modes coexist (see Figure 5.2). We find that the normal SAW mode and the pseudo SAW mode bend away from each other. This resembles an avoided crossing. There is a window of a width of a few degrees in our measurement where both surface modes coexist. A pure SAW mode starts to appear at a lower phase velocity, just below the theoretical bulk phase velocity, and the pseudo SAW starts to quickly fade out. It looks like a split in energy levels due to a coupling between the surface modes. Whether the shear horizontal bulk mode exists in the gap and is involved in the coupling remains unclear. In the actual measurement, we did not measure the bulk mode in the avoided crossing gap.
If there was no coupling, we could probably expect a continuous line for the surface modes that oscillates between a maximum around $\frac{n\pi}{2}$ $(n \in \mathbb{Z})$ and a minimum around $\frac{\pi}{4} + \frac{n\pi}{2}$.

To summarize our results, we observe a good general agreement of our

experimental results with the theoretical model, where we measure the surface modes and several of the bulk modes. The observed avoided crossings in the surface modes could go back to a coupling between them that changes in character over different crystal directions.

Note that apart from the observed avoided crossings, we have also analyzed our FFT without folding quadrants as can be seen in section A.3. This full analysis shows overall good results for $v(\theta)$, but smaller asymmetric deviations up to 0.7 % from the theoretical model that have yet to be explained.

Chapter 6

Conclusion and Outlook

In this thesis, we have measured the acoustic wave modes on the (001) surface of GaAs. We have developed a pipeline to automatically extract the angle-dependent phase velocity $v(\theta)$ from amplitude and phase measurements. Our sample was designed to create omnidirectional waves. Performing a spatial FFT of our amplitude and phase data allowed us to determine the spatial frequencies. Those can be partially associated with different wave modes and the crystal symmetries allowed us to fold the 360° FFT into one 90° quadrant to improve our data quality. Finally, we have calculated $v(\theta)$.

We specifically observed the pure and pseudo SAW modes with their avoided crossing, the longitudinal and the shear horizontal bulk mode. The slight distortions of the $v(\theta)$ modes for the 360°-resolved case with a maximum deviation of 0.7 % remain unclear.

Our setup allows us to investigate scattering caused by the scattering centers, the IDT and edges of our sample. From the dimensions of the scattering centers (d≈1.4 μm) and the wavelength ($\lambda = 2.8\ \mu m$), we conclude that we are in a Mie-like scattering regime which can be further investigated. Having an area of randomly placed scattering centers, interference effects of scattered waves, such as coherent backscattering, can be investigated. Nevertheless, the latter can be at most weakly present in our sample, as we observed weak global scattering effects and the backwards traveling modes in the FFT were spread over a wide angle range.
To better understand what happens at the local level of scattering centers, we could also perform and analyze close-up measurements of our scat-

tering area as we observed highly localized phase jumps and amplitude maxima.

We could further try to qualitatively analyze the coupling of surface waves to bulk waves and where bulk waves are present in our sample. This could provide valuable information when building acoustic cavities as this coupling can lead to a decrease in the Q factor. To learn about the presence of certain bulk modes, we can filter out unwanted signals in the FFT. An inverse Fourier transform returns the amplitude and phase connected to the bulk mode studied.

To improve the focused cavities further, the next step would be to calculate the group velocity v_g to adapt their curvature for a better optomechanical coupling in the focus. Given the good agreement of our theoretical model with the experimental data, one approach for cavity design could be to use the same model to calculate the group velocity.
Furthermore, Msall and Santos show a method how to obtain the group velocity from the phase velocity [15]. In our case, we could model $\mathrm{v}(\theta)$ with a function and go back to spatial frequency space. In this space, we know that $\vec{\mathrm{v}}_\mathrm{p}$ points in the radial direction and the group velocity points in the normal direction of the spatial frequency curves. We can find the angle between both directions for a fixed angle θ. The projection of v_g on the unit vector of the radial direction $\hat{k}$ equals to the magnitude of the phase velocity $\mathrm{v}_\mathrm{p} = \hat{k} \cdot \vec{\mathrm{v}}_g = \mathrm{v}_g \cos\delta$. With this relation, we can then obtain the group velocity.

Finally, when having a model to build better focused cavities, it can also become relevant to make sure that enough waves are actually reflected by the acoustic Bragg mirrors and not transmitted or scattered into other modes. That could, for instance, include considering the thickness out of plane of the Bragg mirror (see [29]) and the amount of layers for high enough reflection.

Version of January 16, 2026– Created January 16, 2026 - 15:59

Acknowledgements

During this project on acoustic waves I have had a great time and learned a lot, but that would not have been possible without support. I would like to thank Thomas who showed me the setup with great patience and guided me through the project as direct supervisor. I appreciate that he took the necessary time to answer my questions and to remind me of important things to remember during the thesis writing. Besides, I was thankful for the weekly meetings with Thomas and Wolfgang, that were very helpful for the progress of the project and further increased my interest in quantum acoustics. I felt very welcome in the research group.

Finally, many thanks to everyone on the ninth floor. I had many interesting and fruitful conversations that sometimes helped me understand new aspects regarding my research.

Bibliography

[1] D. Ilin, "English: A Rayleigh wave / surface acoustic wave (SAW).," Sept. 2020.

[2] D. Royer and E. Dieulesaint, Elastic Waves in Solids I: Free and Guided Propagation. Springer Science & Business Media, 1999.

[3] Y. Xue, Y. Liu, C. Zhou, and X. Y. Zhang, "Acoustic wave devices based on piezoelectric/ferroelectric thin films for high-frequency communication systems and sensing applications," Ceramics International, vol. 50, pp. 52051–52058, Dec. 2024.

[4] P. Delsing, A. N. Cleland, M. J. A. Schuetz, J. Knörzer, G. Giedke, J. I. Cirac, K. Srinivasan, M. Wu, K. C. Balram, C. Bäuerle, T. Meunier, C. J. B. Ford, P. V. Santos, E. Cerda-Méndez, H. Wang, H. J. Krenner, E. D. S. Nysten, M. Weiß, G. R. Nash, L. Thevenard, C. Gourdon, P. Rovillain, M. Marangolo, J.-Y. Duquesne, G. Fischerauer, W. Ruile, A. Reiner, B. Paschke, D. Denysenko, D. Volkmer, A. Wixforth, H. Bruus, M. Wiklund, J. Reboud, J. M. Cooper, Y. Fu, M. S. Brugger, F. Rehfeldt, and C. Westerhausen, "The 2019 surface acoustic waves roadmap," J. Phys. D: Appl. Phys., vol. 52, p. 353001, July 2019. Publisher: IOP Publishing.

[5] P. Chen, G. Li, and Z. Zhu, "Development and Application of SAW Filter," Micromachines, vol. 13, p. 656, May 2022. Publisher: Multidisciplinary Digital Publishing Institute.

[6] Y. Yang, C. Dejous, and H. Hallil, "Trends and Applications of Surface and Bulk Acoustic Wave Devices: A Review," Micromachines, vol. 14, p. 43, Jan. 2023. Publisher: Multidisciplinary Digital Publishing Institute.

[7] D. Mandal and S. Banerjee, "Surface Acoustic Wave (SAW) Sensors: Physics, Materials, and Applications," Sensors, vol. 22, p. 820, Jan. 2022.

[8] N. P. de Leon, K. M. Itoh, D. Kim, K. K. Mehta, T. E. Northup, H. Paik, B. S. Palmer, N. Samarth, S. Sangtawesin, and D. W. Steuerman, "Materials challenges and opportunities for quantum computing hardware," Science, vol. 372, p. eabb2823, Apr. 2021. Publisher: American Association for the Advancement of Science.

[9] A. Vainsencher, K. J. Satzinger, G. A. Peairs, and A. N. Cleland, "Bi-directional conversion between microwave and optical frequencies in a piezoelectric optomechanical device," Appl. Phys. Lett., vol. 109, p. 033107, July 2016.

[10] S. Kumar, N. Lauk, and C. Simon, "Towards long-distance quantum networks with superconducting processors and optical links," Quantum Sci. Technol., vol. 4, p. 045003, July 2019. Publisher: IOP Publishing.

[11] M. Caleffi, L. D'Avossa, X. Han, and A. S. Cacciapuoti, "Quantum Transduction: Enabling Quantum Networking," IEEE Communications Surveys & Tutorials, pp. 1–1, 2025.

[12] P. Steindl, H. Snijders, G. Westra, E. Hissink, K. Iakovlev, S. Polla, J. Frey, J. Norman, A. Gossard, J. Bowers, D. Bouwmeester, and W. Löffler, "Artificial Coherent States of Light by Multiphoton Interference in a Single-Photon Stream," Phys. Rev. Lett., vol. 126, p. 143601, Apr. 2021. Publisher: American Physical Society.

[13] R. A. DeCrescent, Z. Wang, P. Imany, R. C. Boutelle, C. A. McDonald, T. Autry, J. D. Teufel, S. W. Nam, R. P. Mirin, and K. L. Silverman, "Large Single-Phonon Optomechanical Coupling Between Quantum Dots and Tightly Confined Surface Acoustic Waves in the Quantum Regime," Phys. Rev. Applied, vol. 18, p. 034067, Sept. 2022.

[14] R. Takasu, Y. Sato, T. Hata, T. Akiho, K. Muraki, and T. Fujisawa, "Surface-acoustic-wave resonators with Ti, Cr, and Au metallization on GaAs," Appl. Phys. Express, vol. 12, p. 055001, Apr. 2019. Publisher: IOP Publishing.

[15] M. E. Msall and P. V. Santos, "Focusing Surface-Acoustic-Wave Microcavities on Ga As," Phys. Rev. Applied, vol. 13, p. 014037, Jan. 2020.

[16] M. M. de Lima, Jr., F. Alsina, W. Seidel, and P. V. Santos, "Focusing of surface-acoustic-wave fields on (100) GaAs surfaces," J. Appl. Phys., vol. 94, pp. 7848–7855, Dec. 2003.

[17] T. Steenbergen, M. Fisicaro, K. Czerniak, M. Rog, K. Lahabi, and W. Löffler, "Young's double-slit experiment with anisotropic GHz surface acoustic waves on gallium arsenide," Opt. Lett., OL, vol. 50, pp. 6385–6388, Oct. 2025. Publisher: Optica Publishing Group.

[18] M. H. Kuok, S. C. Ng, and V. L. Zhang, "Angular dispersion of surface acoustic waves on (001), (110), and (111) GaAs," J. Appl. Phys., vol. 89, pp. 7899–7902, June 2001.

[19] C. Hwu and W. Becker, "Stroh formalism for various types of materials and deformations," J MECH, vol. 38, pp. 433–444, Mar. 2022.

[20] A. Safari and E. Akdogan, Piezoelectric and Acoustic Materials for Transducer Applications. Springer US, 2008.

[21] P. E. Veefkind, "On Measuring the Spin of Surface Acoustic Waves on GaAs," Master's thesis, Leiden University, 2025.

[22] K. Tanuma, "Stroh Formalism and Rayleigh Waves," J Elasticity, vol. 89, pp. 5–154, Dec. 2007.

[23] D. Royer and E. Dieulesaint, Elastic Waves in Solids II: Generation, Acousto-optic Interaction, Applications. Springer Science & Business Media, 1999.

[24] M. Fisicaro, T. A. Steenbergen, Y. C. Doedes, K. Heeck, and W. Löffler, "Imaging transverse modes in a GHz surface acoustic wave cavity," Aug. 2024. arXiv:2408.11630 [physics].

[25] J. G. Thomas, Z. Xi, J. Ji, G. Shi, B. R. Srijanto, I. I. Kravchenko, Y. Yao, L. Shao, and Y. Zhu, "Spectral interferometry-based microwave-frequency vibrometry for integrated acoustic wave devices," Optica, OPTICA, vol. 12, pp. 935–944, July 2025. Publisher: Optica Publishing Group.

[26] S. Ota, Y. Okazaki, S. Nakamura, T. Oe, H. Sellier, C. Bäuerle, N.-H. Kaneko, T. Kodera, and S. Takada, "Suppression of electromagnetic crosstalk by differential excitation for SAW generation," Appl. Phys. Express, vol. 17, p. 022002, Feb. 2024. Publisher: IOP Publishing.

[27] A. F. Frangi, W. J. Niessen, K. L. Vincken, and M. A. Viergever, "Multiscale vessel enhancement filtering," in Medical Image Computing and Computer-Assisted Intervention — MICCAI'98 (W. M. Wells, A. Colchester, and S. Delp, eds.), (Berlin, Heidelberg), pp. 130–137, Springer, 1998.

[28] E. Meijering, M. Jacob, J.-C. Sarria, P. Steiner, H. Hirling, and M. Unser, "Design and validation of a tool for neurite tracing and analysis in fluorescence microscopy images," Cytometry Part A, vol. 58A, no. 2, pp. 167–176, 2004. _eprint: https://onlinelibrary.wiley.com/doi/pdf/10.1002/cyto.a.20022.

[29] Y. C. Doedes, "Towards Optical Detection of Thermal Phonons in Surface Acoustic Wave Resonators," Master's thesis, Leiden University, 2024.

Appendix A

Appendix

A.1 Amplitude and phase at scattering area

We zoom in to observe one of the bright spots we have discovered on our plots at the scattering areas. Figure A.1 shows such a spot. We can observe it in the amplitude as well as in the phase and the reflectivity. First, the spot diameter can roughly be estimated to be around $2 - 3$ μm. This is close to the SAW wavelength of 2.8 μm and to the actual diameter of the scatterers (1 μm). We can assume that there is actually a scatterer when looking at the reflectivity plot in Figure A.1c. There is a clear difference in reflected power. The amplitude does not only show a much higher value at the scatterer, but also much lower ones in a few spots around it. This indicates a displacement into the plane. Observing the phase also shows strong changes or jumps. Where the amplitude is particularly low, we can

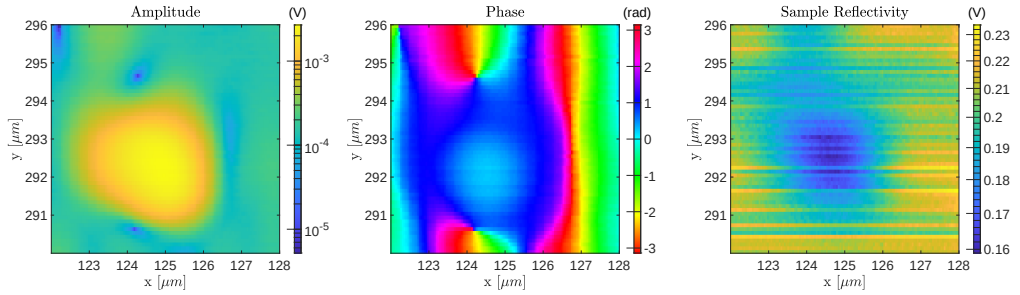

(a) *Amplitude.* ***(b)*** *Phase.* ***(c)*** *Reflected DC power.*

Figure A.1: *Measurement 08. High amplitude spot in scattering area.*

see points of fast phase change. The effect of the scatterers has not been further investigated in this thesis.

A.2 Phase velocity and angle error

There are two considered sources of error that are shown in the $v(\theta)$ plots Figure 5.1.
The pixel error in the FFT stems from the limited area which is available for performing the transform. Often in our measurements, we had more space available in y-direction, thus the pixel step was smaller in y than in x. We denote the pixel error as $\Delta \mathrm{f_x}$ and $\Delta \mathrm{f_y}$. We model a uniform distribution to each bin, which comes down to a standard deviation of $\Delta u_{\mathrm{pixel}} = \frac{\Delta \mathrm{f_{x,y}}}{\sqrt{12}}$ in both directions respectively.
Error propagation of the form

$$(\Delta g(x,y))^2 = \left(\frac{\partial g}{\partial x}\right)^2 (\Delta x)^2 + \left(\frac{\partial g}{\partial y}\right)^2 (\Delta y)^2 + 2\frac{(\partial g)^2}{\partial x \partial y}\mathrm{cov}(x,y) \tag{A.1}$$

can be used. Note that in our case, we have independent variables $\mathrm{f_x}$ and $\mathrm{f_y}$, so $\mathrm{cov}(x,y) = 0$. With the help of error propagation and the equations 4.2, one finds

$$\Delta\theta_i = \sqrt{\left(\frac{\mathrm{f_t}}{\mathrm{f_r^3}}\right)^2 \left((\mathrm{f_x}\Delta u_{\mathrm{pixel},x})^2 + (\mathrm{f_y}\Delta u_{\mathrm{pixel},y})^2\right)} \tag{A.2}$$

$$\Delta \mathrm{v}_i = \sqrt{\left(\frac{1}{\mathrm{f_r^4}}\right) \left((\mathrm{f_y}\Delta u_{\mathrm{pixel},x})^2 + (\mathrm{f_x}\Delta u_{\mathrm{pixel},y})^2\right)} \tag{A.3}$$

with Δ representing the standard deviation and i representing one data point. The averaging over the points in the angle bins further leads to

$$\Delta\bar{\theta}_{px,k} = \sqrt{\frac{\sum m_i^2 \Delta\theta_i}{(\sum m_i)^2}} \tag{A.4}$$

$$\Delta\bar{\mathrm{v}}_{px,k} = \sqrt{\frac{\sum m_i^2 \Delta \mathrm{v}_i}{(\sum m_i)^2}} \tag{A.5}$$

with k the index of a bin.

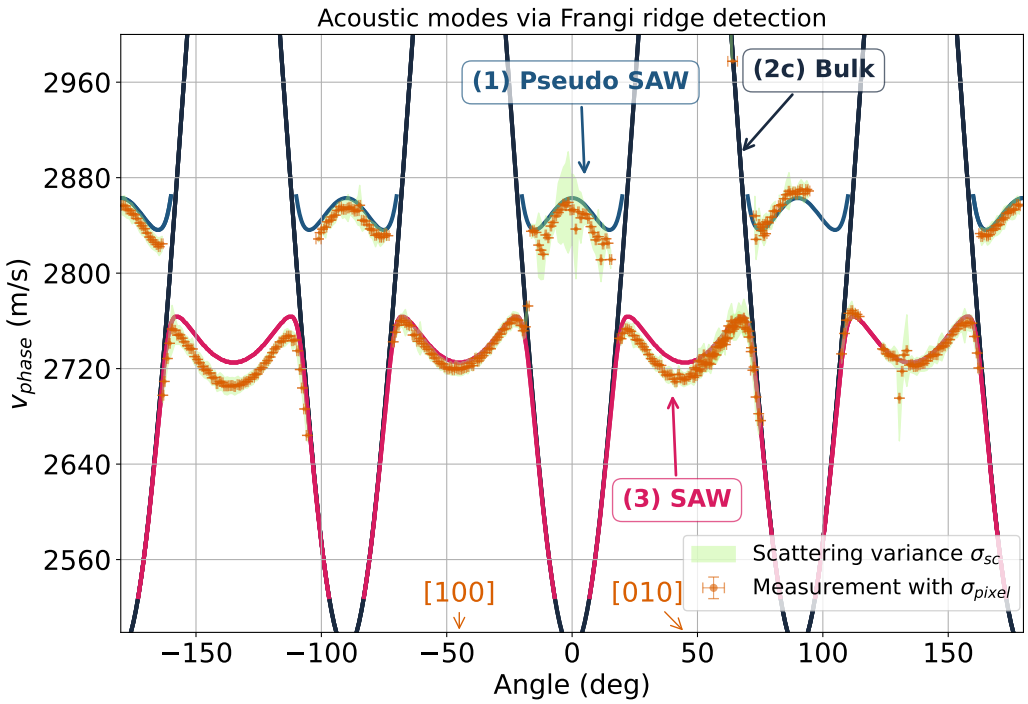

Figure A.2: *$v(\theta)$ of surface modes for all crystal directions with experimental data (in orange) and theoretical model (blue and pink lines). The crystal directions corresponding to the angles are indicated with orange arrows.*

Another measure of uncertainty originates from the averaging which is the geometrical spread of points from the average in each bin k.

$$\Delta\bar{\theta}_{geom,k} = \sqrt{\frac{\sum m_i \cdot (\theta_i - \bar{\theta}_k)^2}{\sum m_i}} \tag{A.6}$$

$$\Delta\bar{\mathrm{v}}_{geom,k} = \sqrt{\frac{\sum m_i \cdot (\mathrm{v}_i - \bar{\mathrm{v}}_k)^2}{\sum m_i}} \tag{A.7}$$

The standard deviations have been represented on the plots in chapter 5, where σ_{pixel} stands for errors originating from the pixels and σ_{sc} stands for the geometrical spread error (see for instance Figure 5.1).
In the majority of associated errors, they were relatively small, but could also not provide further insight into deviations observed in chapter 5.

Version of January 16, 2026– Created January 16, 2026 - 15:59

A.3 Symmetries for $360°$

So far, we have only considered averaged data of the FFT quadrants folded into one. We can also consider the full circle and make some interesting observations on the surface modes (see Figure A.2).

Although our measured modes fit the model quite well, we observe data points that deviate slightly from the model. The pseudo SAW in the [110] direction, or $0°$, simply causes spectral leakage and high magnitude noise which is taken up by the ridge detection method and therefore the obtained points have a higher geometrical spread and do not fit the model as well as in other parts.
However, there are also surface modes in other directions, that deviate from the model. The largest deviation (see Figure A.2) is around $-135°$ with 20 ms^{-1} lower than in the model. The quadrants on the top right ($0° - 90°$) and on the bottom left ($-180°$ to $-90°$) deviate the most. The degree of deviation also varies within the quadrants and we cannot see a symmetry pattern. The experimental investigations into these deviations have not been part of this project and have not lead to a conclusive explanation yet.

We have also considered the precision of the data extraction through the ridge detection process as potential source of the deviations. For that, we estimated the required distance between a detected point and the center of the ridge to cause a 20 ms^{-1} deviation of the phase velocity. When observing the overlap of brightest magnitude and detected points, there always seemed to be a good overlap and a ridge with a width of a few pixels. We can make an estimate for our measurement to see whether detected pixels that are more on the side of the ridge could cause a large enough deviation.

The size of pixels is $\Delta f_{x,pixel} = 0.0007712\,\mu m^{-1}$ and $\Delta f_{y,pixel} = 0.000769\,\mu m^{-1}$. We recall that $v = \frac{f_t}{\sqrt{f_x^2+f_y^2}} = \frac{f_t}{f_s}$ and from there we get

$$\Delta f_s = \frac{f_t}{v + \Delta v} - \frac{f_t}{v} \tag{A.8}$$

which allows to calculate the spatial frequency deviation in the radial direction of the FFT for a chosen phase velocity.

We consider the mode with the largest experimental deviation from the model at $\theta = -135°$ (see Figure A.3a).

Version of January 16, 2026– Created January 16, 2026 - 15:59

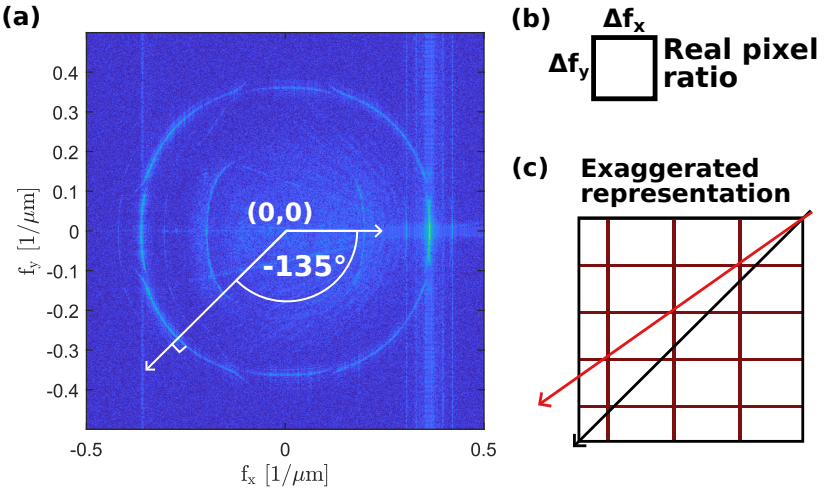

Figure A.3: *(a) FFT with arrows indicating the direction of largest deviation in found phase velocity, the horizontal axis direction and the angle between them. (b) Enlarged representation of pixel with correct ratio. (c) Square filled with rectangular pixels with pixel diagonal in red and square diagonal in black to show the different directions of square and pixel diagonal in an exaggerated manner.*

- v= 2700 ms^{-1} and $\Delta v = -20\ ms^{-1}$
- Then, $\Delta f_s \approx -0.00285\ \mu m^{-1}$ ($f_t = 1.03205$ GHz).

We note that our pixels are nearly square as $\Delta f_{x,pixel} \approx \Delta f_{y,pixel}$ (see Figure A.3b). The angle we consider ($\theta = -135°$) is spanned by the horizontal axis and the perpendicular through the FFT line, that can also said to be 45° away from the horizontal axis. There is a negligible deviation of the pixel diagonal direction from the direction of this perpendicular.

- Angle of pixel diagonal (with horizontal axis): $\arctan\left(\frac{\Delta f_{y,pixel}}{\Delta f_{x,pixel}}\right) = 44.9...° \approx 45°$
- The measured deviation in diagonal pixel steps: $\frac{\Delta f_s}{\sqrt{(\Delta f_{x,pixel})^2+(\Delta f_{y,pixel})^2}} = 2.6168... \approx 2.6$

This is around half of the width of the usually detected ridge along the pixel diagonal. However, we have never observed that points of the detected ridge deviate that strongly from the highest magnitude. Only smaller deviations in the phase velocity could perhaps partially be caused by the extraction method as a 5 ms^{-1} deviation corresponds to a 0.65 pixel steps.

The largest deviation corresponds roughly to a $\frac{20\ ms^{-1}}{2700\ ms^{-1}} \approx 0.7$ % deviation.

This is still less than in the surface mode measurements of Kuok, where deviations of 2.5 % or larger were found [18].